Proceedings Paper:
Pang, B., Zhao, Y. and Yang, S. (2025) Data-Driven Calibration for Wearable Brain Functional Imaging Devices. In: 2025 IEEE Congress on Evolutionary Computation (CEC). 2025 IEEE Congress on Evolutionary Computation (CEC), 08-12 Jun 2025, Hangzhou, China. Institute of Electrical and Electronics Engineers (IEEE). ISBN: 979-8-3315-3431-8.

https://doi.org/10.1109/cec65147.2025.11043082

Data-Driven Calibration for Wearable Brain Functional Imaging Devices

Beiyin Pang
School of Mechanical Engineering
University of Leeds
Leeds, UK
B.Pang@leeds.ac.uk

Yunyi Zhao
Division of Surgery and Intervention Science
University of College London
London, UK
Yunyi.Zhao.21@UCL.ac.uk

Shufan Yang
School of Mechanical Engineering
University of Leeds
Leeds. UK
S.F.Yang@leeds.ac.uk

***Abstract*—Recent advancements in near-infrared spectroscopy (NIRS) and associated optical techniques have significantly contributed to the development of wearable neuroimaging devices capable of capturing real-time neuronal activity with enhanced spatial and temporal resolution. However, despite these advancements, calibration remains a persistent challenge due to variability in NIRS sensor design, which can significantly degrade data quality. In this paper we introduce a universal data-driven calibration method designed to enhance the precision and reliability of NIRS sensor measurement. The proposed method integrates gradient descent–based optimisation with constraint-guided clustering to iteratively minimise calibration errors under realistic usage conditions. To evaluate its effectiveness, the algorithm was tested using an in-silico phantom constructed in MATLAB/NIRFAST, demonstrating notable improvements in signal clarity and haemoglobin concentration estimation. Additionally, the approach exhibits robustness to motion artefacts, thereby improving measurement fidelity. These contributions advance the reliability and accessibility of wearable brain imaging systems, enabling broader applications in both neuroscience research and clinical diagnostics.**

Keywords— fNIRS, constraint-based clustering, optimisation

I. INTRODUCTION

Functional Near-Infrared Spectroscopy (fNIRS) is a non-invasive, mobile brain imaging method that uses optical methods to study regional oxygen consumption in the brain [1]. Calibration is a crucial step in fNIRS devices to ensure the accuracy, reliability, and validity of the data collection during neuroimaging reconstruction. Traditional calibration of wearable device using a spectrophotometer in an optical phantom is typically performed by utilising a small set of representative samples to model the systematic difference between measured and reference value [2, 3]. However, many existing methods fail to account for potential sources of spectral deviation. Factors such as noise, sample heterogeneity, variations in optical sensor placement, difference in the optical path can introduce inaccuracies in absorption measurement within the brain tissue, ultimately degrading the overall measurement accuracy [4].

Data-driven calibration has become a widely accepted technology in various applications due to its effectiveness in addressing complex instrumental errors [5, 6]. However, data-driven calibration for Near-Infrared Spectroscopy (NIRS) wearable devices is challenging because of the high variability in real-world conditions (colour of hair, brain anatomy, motion artifacts), meanwhile the difficulty of collecting large, high-quality labelled datasets is a barrier to applying data-driven calibration. In this paper, we present a data-driven calibration methodology leveraging machine learning optimisation to address the identified challenges. The proposed approach incorporates a constraint-based clustering algorithm using synthetic data and further refines through a gradient descent-based optimisation approach to enhance its precision and reliability. The primary advantage of a data-driven calibration approach lies in its ability to adaptively reduce noise while also preserving shifts in the detected spectrum. Unlike traditional hardware-based calibration, data-driven calibration continuously updates its coefficients based on the pre-trained constraints and clustering techniques, enabling adaptive adjustment of filter coefficient parameters. We evaluated our approach on customised designed NIRS sensor with two channels operating at 670nm wavelength and 810nm. We employed a meshed three-dimensional(3D) head model with a Jacobian matrices index to demonstrate the effectiveness of drift and noise correction in NIRS signals using this novel data-driven calibration method. These advancements significantly enhance the accuracy and reliability of NIRS measurements.

The main contributions of this paper are as follows: (1) the development and demonstration of a data-driven calibration utilising a machine learning optimisation to enhance calibration accuracy; and (2) the introduction of a theoretical framework for evaluating improvements in signal integrity by introducing Jacobian matrices index on 3D meshed brain simulation.

II. MATERIALS AND METHOD

A. Overview of NIRS

While a conventional NIRS sensor provides a static 'snapshot' of tissue oxygenation, NIRS sensor can also be used to capture dynamic time-series data across multiple NIRS source–detector pairs as the human engages in specific task. By quantifying task-evoked changes in oxyhaemoglobin (HbO) and deoxyhaemoglobin (HbR) concentrations—indicative of neurovascular coupling—NIRS enables the generation of spatially resolved hemodynamic activation maps [1, 7, 8].

The Beer-Lambert Law (BLL) describes how the attenuation of light through a medium depends on its properties. The modified BLL (MBLL) extends this principle to account for light scattering, which is significant in biological tissues [9]. The law is mathematically represented as:

$$A(t,\lambda) = -log(\frac{I(t,\lambda)}{I_0(t,\lambda)}) = \sum_{i=1}^{n} \epsilon_{i\lambda} c_i(t) DPF(\lambda) d + G(\lambda) \quad (1)$$

where: $A(t,\lambda)$ is the attenuation at time t and wavelength λ; I_0 is incident intensity on the sample at time t and wavelength λ ; $c_i(t)$ is concentration of the i -th chromophore at time t in mol; $\epsilon_{i\lambda}$ is molar extinction

979-8-3315-3431-8/25/$31.00 ©2025 IEEE

coefficient of the i -th chromophore at wavelength λ; and DPF(λ) is differential pathlength factor at wavelength λ;G(λ) is scattering dependent light intensity loss parameter at wavelength λ.

Local neural activity and the subsequent changes in cerebra blood flow are used to calculate the hemodynamic response of brain region activities, which indicate HbO begins to rise within 1-2 seconds.

B. Experimental Data Collection

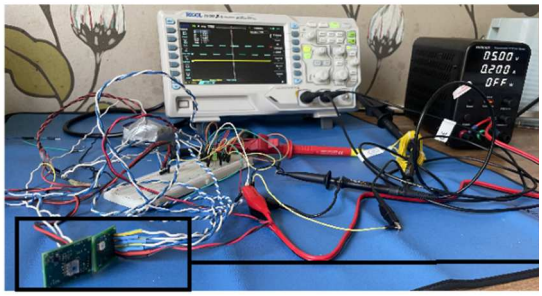

Fig. 1 The benchtop setup. It includes the source-detector pair -enclosed within the marked black box, a voltmeter and digital oscillator, which used to evaluate circuit performance and signal integrity.

In this project, two datasets were utilised. The first dataset was collected using an in-house NIRS sensor, where participants performed a hand-clenching task by clutching their hands for 10 seconds followed by a release. Each participant takes 10 trials. The resting dataset was used from a public available dataset [10]. Fig. 1 provides a detailed illustration of the experimental set-up for NIRS data collection. The devices employed in this study operated using the continuous wave method. Therefore, the differential path length factor (DPF) could not be measured directly. Instead, it was estimated using experimental value [4].

C. Function of Data-driven Calibration

The proposed calibration algorithm updates the filter coefficients recursively to minimise the squared error between outputs. This method adapts dynamically to new data points, allowing for rapid convergence and effective handling of variations in input statistics using a gradient descent-based method. The adaptability of the gradient descent-based method allows the data acquisition system to effectively handle variations in input statistics and rapidly converge to optimal coefficients [11]. A Kalman Filter (KF) is used to estimate the state of a dynamic system from noisy measurements by predicting and updating states to minimise the squared error. Traditional KFs assume fixed noise statistics [12].

As illustrated in Fig. 2, after preprocessing, the changes in oxy-haemoglobin (ΔHbO) and deoxy-haemoglobin (ΔHbR) concentrations are computed from the optical density data. These time series reflect how haemoglobin levels vary relative to the resting state baseline. The red dashed lines indicate information flowing from the hardware-based Calibration (and resting-state data) into the filter selection process, ultimately producing the filtered outputs.

The blue arrows within the green box illustrate an internal feedback loop among different methods (constrained-clustering, gradient-descent optimisation) with iterative techniques. The data-driven algorithm employs a straightforward iterative approach to regulate filter coefficients, making it suitable for implementation in real-time processing environments. This real-time capability enables researchers to observe the effects of minimising unwanted spectral deviation, facilitating more accurate analysis of fNIRS signals.

The mathematical expression of the data-driven calibration, shown in Eq. (2), (3) and (4) share a structure similar to the original formulas proposed by Widrow et al.[13]. For this work, we adapted those formulas to align with gradient decent optimisation.

$$y(t) = w^T(t)x(t) \tag{2}$$

where: $y(t)$ is the output of the filter at time t; $w(t) = [w_0(t)\ w_1(t)\ \dots\ w_{n-1}(t)]^T$ is the vector of filter coefficients at time t, where n is the filter order; $x(t) = [x(t)\ x(t-1)\ \dots\ x(t-n+1)]^T$ is the input vector at time .

$$e(t) = d(t) - y(t) \tag{3}$$

where: $e(t)$ is the error signal at time t; $d(t)$ is the desired signal at time t.

$$w(t+1) = w(t) + \mu\, x(t)e(t) \tag{4}$$

where: $w(t+1)$ is the updated coefficient vector; μ is the step size (learning rate) for gradient descent of the algorithm. The convergence condition is

$$0<\mu<2/\lambda_{max}$$

Where λ_{max} is the largest eigenvalue of the input signals' autocorrelation matrix.

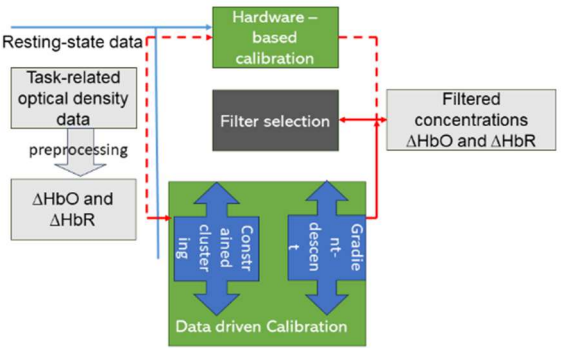

Fig 2. Data flow and system overview

The key part of data-driven calibration is shown in the pseudo-code Algorithm I. The implementation process comprised the following steps:

1. Adjustment of the parameters: The selected filter parameters were determined by the noise type of each channel. For instrumental noise, the following parameters were selected: A moderate step size of μ = 0.01 and filter order of 10 were selected to accommodate stable yet consistent noise patterns. Physiological noise: A smaller step size (μ = 0.005) and a higher filter order (20) were employed in order to capture complex, low-frequency noise. In the case of a normal signal, a larger step size (μ = 0.02) and a lower

filter order (5) were selected, reflecting minimal noise interference.

2. Filter Application: The filter coefficients were modified in real time in order to minimise the mean square error between the desired and actual signals, thereby replacing the original noisy signal with a filtered version.

3. Error Calculation and Coefficient Update: This process guaranteed that the filter would remain responsive to changing measurement conditions.

Subsequently, the filtered signals were subjected to processing through the MBLL, whereby optical density changes were converted into corresponding changes in haemoglobin concentration. This integration enhanced the accuracy and integrity of the data by reducing the impact of noise on the final measurements.

```
Algorithm I: Data_Driven_Calibration

Procedure Data_Driven_Calibration(rawSignal,
desiredSignal, learningRate, filterOrder, maxIterations)
 if length(rawSignal) = 0
      return "No data"
   # Initialize filter coefficients and sample buffer with
cluster processing data
   w[1..filterOrder] = 0
   x[1..filterOrder] = 0
   # Adapt filter coefficients
   for iter = 1 to maxIterations:
      for n = 1 to length(rawSignal):
         # Shift x, then insert new sample
         for i = filterOrder down to 2:
            x[i] = x[i-1]
         x[1] = rawSignal[n]
         # Compute output and error
         y = 0
         for i = 1 to filterOrder:
            y += w[i] * x[i]
         error = (desiredSignal != empty) ?
(desiredSignal[n] - y) : -y
         # Update coefficients
         for i = 1 to filterOrder:
            w[i] += learningRate * error * x[i]
   # Generate final calibrated signal
   calibratedSignal = array(length(rawSignal))
   x[1..filterOrder] = 0
   for n = 1 to length(rawSignal):
      for i = filterOrder down to 2:
         x[i] = x[i-1]
      x[1] = rawSignal[n]
      outVal = 0
      for i = 1 to filterOrder:
         outVal += w[i] * x[i]
      calibratedSignal[n] = outVal
   return calibratedSignal
EndProcedure
```

III. Results

A. Experimental Setting

The fNIRS data used in this paper were sourced from publicly available resting-state datasets [14] and grand truth used in [15]. Due to the large number of channels included in the data, some were visibly inconsistent with resting-state conditions. Thus, a preprocessing step was implemented to select stable channels representing the resting state.

Constraint-based clustering automatically classifies and adapts different types of noise, enabling dynamic parameter adjustment. The training of constraint-based clustering uses synthetically generated noise, including five types of noise: white noise, Gaussian noise, step function noise, triangle noise and pink noise. White noise represents instrumental noise. It often originates from random electronic fluctuations within the fNIRS device and introduces variability to the signal, thereby obscuring genuine hemodynamic changes. Common in both instrumental and environmental contexts, Gaussian noise follows a normal distribution, with most noise values clustering around a mean. This probabilistic nature complicates the detection of subtle hemodynamic responses, thereby reducing measurement precision. Pink noise also known as 1/f noise, features a power spectrum with greater intensity at lower frequencies, reflecting slow physiological processes such as blood flow fluctuations and metabolic rhythms. Its presence in fNIRS data as underlying biological rhythms that contribute to hemodynamic responses. Step function noise is associated with motion artifacts, arising from abrupt signal changes caused by sudden subject movements, such as head shifts or probe adjustments. These artifacts disrupt the optical path length, causing transient signal distortions. Triangle noise can represent systematic patterns, such as mechanical movements or physiological cycles, like breathing. Regular, repetitive movements modulate the optical signals, generating triangle waveforms in the data.

The data-driven calibration method was systematically integrated into the Modified Beer–Lambert Law (MBLL) function within Homer3, an open-source neuroimaging analysis toolbox developed and maintained by the Boston University Neurophotonics Center [10]. Specifically, the calibration procedure was embedded in the modified hmrR_OD2Conc function, wherein it is applied to the optical time-series data prior to the conversion from optical density to chromophore concentration changes.

```
% Implementing adaptive filtering on the data
for ch = 1:size(y, 2)
    % Adaptive filtering using LMS filter example
    mu = 0.01; % Step size for LMS
    nOrder = 10; % Filter order
    h = zeros(nOrder, 1); % Initial filter coefficients
    for t = nOrder:nTpts
        x = y(t:-1:t-nOrder+1, ch); % Input vector for filter
        d = y(t, ch); % Desired signal
        y_hat = h' * x; % Filter output
        e = d - y_hat; % Error signal
        h = h + mu * x * e; % Update filter coefficients
        y(t, ch) = y_hat; % Replace original signal with filtered
    end
end
```

Fig. 3. The source code for constrained clustering for data-driven calibration approach in hmrR_OD2Conc function

An illustrative code excerpt demonstrating this implementation is presented in Fig. 3. This preprocessing step is designed to minimise signal noise and variability. The implementation process involves several critical stages, beginning with the specification of filter parameters, such as filter order and step size. Subsequently, filter coefficients are iteratively updated in accordance with the characteristics of the input signal. The original time-series data are then

replaced with the filtered output, resulting in a significant reduction in signal deviation and enhanced signal fidelity for concentration computation. The result of data features using clustering method is shown in Fig.4.

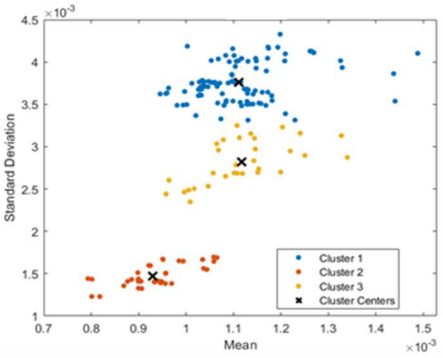

Fig. 4 Clustering Results of NIRS data

B. *Clustering analysis*

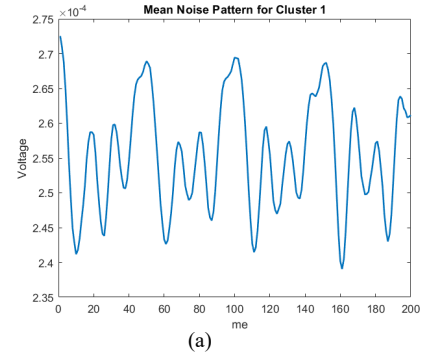

(a)

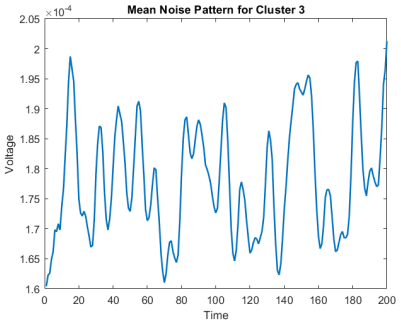

(b)

Fig. 5 The clustering features of NIRS signals.
(a) Cluster1 feature. (b) Cluter2 feature.

Improper modification of filter coefficient parameters can result in signal distortion, which highlights the need for effective parameter optimisation [19]. Because NIRS data often includes dynamic changes over time, a sliding window technique is used to segment the data. This involves dividing the data into overlapping windows with a specified 'window_size' and 'step_size'. The sliding window method can focus on localised patterns within each segment [15, 16], the process calculates statistical features, which include the mean and standard deviation for each segment. By analysing the extracted features, the method employs constraint-based clustering to group the data windows into different clusters. And the number of clusters here is set to three, which assumes the dataset includes distinct patterns, such as unlinked signals and actual signals. The clustering method helps to sort the data based on similarities in their statistical properties.

The data pattern in Cluster 1 in Fig.5 shows regular fluctuations in amplitude, suggesting a periodic character similar to physiological data, such as breathing or heartbeats, which exhibit smoother transitions and regular intervals. In contrast, Cluster 3 displays more erratic amplitude changes, indicating environmental light inference or instrumental. Environmental noise can come from surrounding sounds or vibrations, while instrumental noise may result from electrical interference or equipment vibrations. These patterns are more irregular and lack periodicity, distinguishing them from the smoother, rhythmic physiological data. Thus, Cluster 1 is likely physiological data, and Cluster 3 represents environmental stray light caused crosstalk. Unlike current researchers only focus on the physiological signals that they are interested in. This approach is particularly beneficial in including environmental noise due to device limitations or external factors.

C. *Quality Evaluation within Homer3*

The improved performance of signal deviation in Homer3 using data-driven calibrations is evidence in Fig. 6. The upper panel shows the raw signal prior to the implementation of calibration techniques, while the lower panel illustrates the signal after applying the data-driven calibration technique.

The unfiltered signal (upper diagram) shows fluctuations and noise artifacts at 118s, with baseline drift that can obscure key findings of neuroactivities. This baseline drift likely originates from instrumental or physiological sources, complicating the interpretation of hemodynamic responses, thus resulting in the wrong presentation of neural activities. As seen in the second plot, the signal becomes smoother and more regular, with reduced amplitude fluctuations. This indicates reduced signal deviation, allowing for accurate neural activity representation. This is crucial to ensuring that subtle variations in HbO and HbR concentrations are not obscured by noise, thereby enabling researchers to accurately measure changes in brain activities using NIRS.

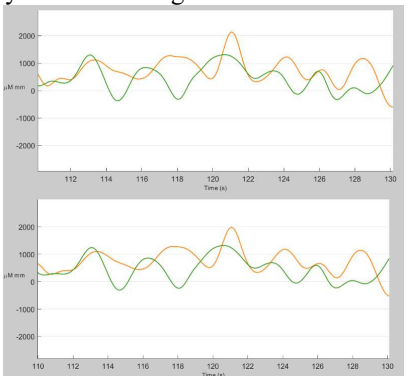

Fig. 6: Concentration change of HbO of a paired source-detector (green line indicates HbR and yellow line HbO)

D. *In-Silicon Phantom for Enhanced fNIRS Data Analysis*

For evaluating enhanced simulation and parameter optimisation in fNIRS, we create 3D meshes from segmented brain CT scans. Each anatomical feature relevant

to the study, such as the skull, skin, grey matter, and white matter, is segmented to reflect its unique optical properties. The segmented images are used to generate a tetrahedral mesh, ensuring that the mesh accurately represents the complex geometries of the human head, as shown in Fig. 7. Parameters such as tetrahedron size is 5mm and the quality is 5 to balance between computational efficiency and simulation accuracy.

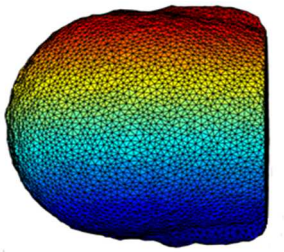

Fig. 7 3D meshed head mode

Following mesh creation, each tissue type, properties such as HbO and HbR concentration, water fraction, scatter amplitude, and scatter power are assigned based on empirical data [17], shown in Table I.

TABLE I. OPTICAL PROPERTIES OF DIFFERENT HEAD LAYERS

	HbT (mM)	***So2 (%)***	***Water (fraction)***	***Scatter Amplitude***	***Scatter Power***
Skin	0.06	75	0.5	2	0.5
Bone	0.049	80	0.15	1.4	1.4
CSF	0.001	90	0.99	0.5	0.2
White Matter	0.076	71	0.78	0.76	0.54
Grey Matter	0.076	71	0.78	0.76	0.54

This simulation is designed to evaluate the improvements achieved through data driven calibration enhancement. First, boundary data is generated using the Finite Element Method. Boundary data is generated for different wavelengths of NIR light. This data forms the basis for analysing light propagation and absorption in the tissue. To test the robustness of the simulation framework, hypoxic conditions are modelled by systematically altering the oxygenation levels within the brain regions in the mesh. This part of the simulation helps in understanding how changes in brain oxygenation could be detected and quantified using the data-driven calibration approach.

In this paper, we utilise Jacobian matrices as the evaluation matrix for indicating changes in light intensities to variations in tissue properties, enabling a detailed analysis of light absorption based on a calibration method. This mathematical model quantifies how changes in tissue properties affect light absorption and scattering, improving the accuracy of calculating changes of blood flow to the brain region.

The relationship between light intensity and tissue chromophore concentrations can be expressed as:

$$\Delta I = J \,.\, \Delta C \tag{5}$$

Where ΔI: Measured changes in light intensity at the detectors. J: Jacobian matrix, describing the sensitivity of light intensity to changes in chromophore concentrations. ΔC Changes in chromophore concentrations (HbO and HbR).

For a given optical measurement system in Eq. 5, Where, I_1,I_(2,…,) I_n are light intensity at n detectors:

$$A = \begin{bmatrix} \frac{\partial I_1}{\partial HbO_1} & \cdots & \frac{\partial I_1}{\partial HbR_1} \\ \vdots & \ddots & \vdots \\ \frac{\partial I_n}{\partial HbO_n} & \cdots & \frac{\partial I_1}{\partial HbR_n} \end{bmatrix} \tag{6}$$

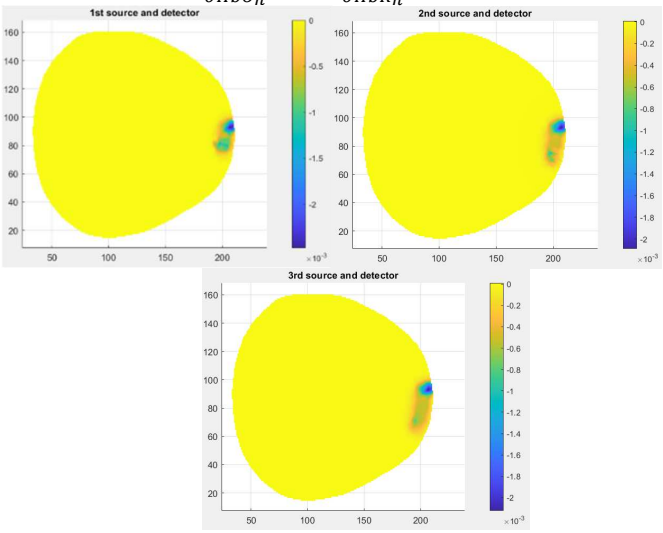

Fig. 8 Changes in tissue oxygenation in Jacobian matics at source-detect pair

The application of Jacobian matrices in simulations allows for controlled adjustments of noise variables, effectively demonstrating how data-driven calibration techniques can be incorporated. Fig. 8 illustrates the results of using Jacobian matrices to analyse changes in the concentrations of tissue oxygenation index (TOI), which defined in eq.(7).

$$TOI = \frac{HbO}{HbO+HbR} \tag{7}$$

The colour scale represents the magnitude of changes in tissue oxygenation. The blue colour indicates a decrease in oxygenation in that point. In this project, we only use one pair of detector and source, so the majority of the tissue area shows no change in oxygenation (highlighted in yellow). The spatial difference in the detected changes across the three subplots is due to the varying distance between source and detector pairs. The variability demonstrates the data-driven calibration successfully captured measurable changes in oxygenation.

IV. CONCLUSION

This paper presents the development and validation of a data-driven calibration algorithm designed to enhance the quality of NIRS data. The integration of a data-driven calibration approach presents a significant advancement in fNIRS measurements by introducing a machine learning optimisation capable of effectively correcting baseline drifts in NIRS signals. This innovative method improves the precision of optical measurement, facilitating more accurate interpretations of neural activities.

Another accomplishment was the development of a digital in-silico phantom using MATLAB/NIRFAST [18]. This model enabled the simulation of NIRS signal acquisition under various controlled conditions, serving as a versatile tool for testing and refining the methodologies

developed in this project. While not directly employed to validate the adaptive algorithm, the in-silico phantom

V. FUTURE WORK

Future work should focus on exploring advanced filtering algorithms to enhance real-time mitigation methods for baseline shift reduction strategies in various sensors. Integrating these algorithms into existing NIRS frameworks could improve the system's ability to manage variations, thereby increasing the precision of detecting subtle HbO and HbR concentration changes. Additionally, expanding the validation of the data driven calibration using diverse experimental datasets will be essential to strengthen its generalisability. Validation across various experimental conditions will ensure the robust applicability of the algorithm, facilitating its adoption in a wide range of fNIRS applications.

REFERENCES

[1] H. Y. Kim, K. Seo, H. J. Jeon, U. Lee, and H. Lee, "Application of functional near-infrared spectroscopy to the study of brain function in humans and animal models," *Molecules and cells,* vol. 40, no. 8, pp. 523-532, 2017.

[2] R. N. Feudale, N. A. Woody, H. Tan, A. J. Myles, S. D. Brown, and J. Ferré, "Transfer of multivariate calibration models: a review," *Chemometrics and intelligent laboratory systems,* vol. 64, no. 2, pp. 181-192, 2002.

[3] Y. Yamashita, A. Maki, and H. Koizumi, "Wavelength dependence of the precision of noninvasive optical measurement of oxy-, deoxy-, and total-hemoglobin concentration," *Medical physics,* vol. 28, no. 6, pp. 1108-1114, 2001.

[4] D. T. Delpy, M. Cope, P. van der Zee, S. Arridge, S. Wray, and J. Wyatt, "Estimation of optical pathlength through tissue from direct time of flight measurement," *Physics in Medicine & Biology,* vol. 33, no. 12, p. 1433, 1988.

[5] J. J. Workman Jr, "A review of calibration transfer practices and instrument differences in spectroscopy," *Applied spectroscopy,* vol. 72, no. 3, pp. 340-365, 2018.

[6] S. Bandyopadhyay, R. Hamerly, and D. Englund, "Hardware error correction for programmable photonics," *Optica,* vol. 8, no. 10, pp. 1247-1255, 2021.

[7] X. Zhou *et al.*, "Review of recent advances in frequency-domain near-infrared spectroscopy technologies," *Biomedical Optics Express,* vol. 14, no. 7, pp. 3234-3258, 2023.

[8] H. R. Al-Omairi, S. Fudickar, A. Hein, and J. W. Rieger, "Improved Motion Artifact Correction in fNIRS Data by Combining Wavelet and Correlation-Based Signal Improvement," *Sensors,* vol. 23, no. 8, p. 3979, 2023.

[9] W. B. Baker, A. B. Parthasarathy, D. R. Busch, R. C. Mesquita, J. H. Greenberg, and A. Yodh, "Modified Beer-Lambert law for blood flow," *Biomedical optics express,* vol. 5, no. 11, pp. 4053-4075, 2014.

[10] T. J. Huppert, S. G. Diamond, M. A. Franceschini, and D. A. Boas, "HomER: a review of time-series analysis methods for near-infrared spectroscopy of the brain," *Applied optics,* vol. 48, no. 10, pp. D280-D298, 2009.

[11] H.-D. Nguyen, S.-H. Yoo, M. R. Bhutta, and K.-S. Hong, "Adaptive filtering of physiological noises in fNIRS data," *Biomedical engineering online,* vol. 17, pp. 1-23, 2018.

[12] F. Scholkmann *et al.*, "A review on continuous wave functional near-infrared spectroscopy and imaging instrumentation and methodology," *Neuroimage,* vol. 85, pp. 6-27, 2014.

[13] B. Widrow, "Adaptive noise canceling: Principles and applications," *Proc. IEEE,* vol. 63, pp. 1707-1709, 1975.

[14] A. von Lühmann, X. Li, N. Gilmore, D. A. Boas, and M. A. Yücel, "Open access multimodal fNIRS resting state dataset with and without synthetic hemodynamic responses," *Frontiers in Neuroscience,* vol. 14, p. 579353, 2020.

[15] M. Aqil, K.-S. Hong, M.-Y. Jeong, and S. S. Ge, "Cortical brain imaging by adaptive filtering of NIRS signals," *Neuroscience Letters,* vol. 514, no. 1, pp. 35-41, 2012.

[16] Y. Huang, F. Zhu, G. Jia, and Y. Zhang, "A slide window variational adaptive Kalman filter," *IEEE Transactions on Circuits and Systems II: Express Briefs,* vol. 67, no. 12, pp. 3552-3556, 2020.

[17] M. Jia *et al.*, "Quantitative Method for Liquid Chromatography–Mass Spectrometry Based on Multi-Sliding Window and Noise Estimation," *Processes,* vol. 10, no. 6, p. 1098, 2022.

[18] H. Dehghani *et al.*, "Near infrared optical tomography using NIRFAST: Algorithm for numerical model and image reconstruction," *Communications in numerical methods in engineering,* vol. 25, no. 6, pp. 711-732, 2009.

[19] Y. Zhao, Y. Xia, R. Loureiro, H. Zhao, U. Dolinsky, and S. Yang, "FPL Demo: A learning-based motion artefact detector for heterogeneous platforms," in *Proc. 33rd Int. Conf. Field-Programmable Logic and Applications (FPL)*, Gothenburg, Sweden, 2023, pp. 366, doi: 10.1109/FPL60245.2023.00071.